UC Berkeley
UC Berkeley Previously Published Works

Title

Recording interfacial currents on the subnanometer length and femtosecond time scale by terahertz emission

Permalink

Journal

ISSN

Authors

Yue, Eric
Guzelturk, Burak
Li, Guoqing
et al.

Publication Date

DOI

Copyright Information

Peer reviewed

Recording interfacial currents on the subnanometer length and femtosecond time scale by terahertz emission

Eric Yue Ma[1,2]*, Burak Guzelturk[2,3]*, Guoqing Li[4], Linyou Cao[4], Zhi-Xun Shen[1,2], Aaron M. Lindenberg[2,3], Tony F. Heinz[1,2]†

Electron dynamics at interfaces is a subject of great scientific interest and technological importance. Detailed understanding of such dynamics requires access to the angstrom length scale defining interfaces and the femtosecond time scale characterizing interfacial motion of electrons. In this context, the most precise and general way to remotely measure charge dynamics is through the transient current flow and the associated electromagnetic radiation. Here, we present quantitative measurements of interfacial currents on the subnanometer length and femtosecond time scale by recording the emitted terahertz radiation following ultrafast laser excitation. We apply this method to interlayer charge transfer in heterostructures of two transition metal dichalcogenide monolayers less than 0.7 nm apart. We find that charge relaxation and separation occur in less than 100 fs. This approach allows us to unambiguously determine the direction of current flow, to demonstrate a charge transfer efficiency of order unity, and to characterize saturation effects.

INTRODUCTION

Much of modern technology from electronic and optoelectronic devices for information processing (1, 2) to solar cells (3) and batteries (4) depends on the movement of electrons across interfaces. The intrinsic spatial and temporal scales for these charge transfer processes are defined by the angstrom length scale of the interface and the corresponding femtosecond time scale for interfacial electron motion (5). Few measurement techniques are available to probe these scales simultaneously. Although spectroscopic analysis of transient material response [e.g., optical pump-probe spectroscopy (5, 6)] can access this time scale using femtosecond lasers, this approach requires detailed spectroscopic signatures of the materials involved and can be difficult to interpret in the presence of competing relaxation channels such as energy transfer (7).

On the other hand, measurement of the time variation of the radiated electric fields provides a quantitative method for determining the magnitude and temporal variation of the source currents (8). Unlike transient analyses of material response, this approach can be applied in a very general fashion without the need for detailed spectroscopic information about the materials involved. It is, moreover, robust against competing charge-neutral relaxation processes (7). The method can be readily implemented using time-domain terahertz (THz, 10^{12} Hz) emission spectroscopy (TES) (9, 10), in which the electric field waveform is directly recorded following excitation of the sample by an ultrashort optical pulse. The approach has been successfully applied to probe ultrafast electron dynamics in a variety of gaseous (11), liquid (12), and solid-state systems (13–15).

In the context of interfacial charge transfer, TES provides direct access to the femtosecond time scale but was commonly thought to lack sufficient sensitivity to record subnanometer interfacial currents. We note, however, that if 10^{12} electrons per cm^2 move in the out-of-plane direction over a distance $d = 0.5$ nm (in vacuum) within 100 fs, the resulting electric field strength E near the sheet (for $\theta = 45°$ emission) would be ~15 V cm^{-1}, a small but readily accessible value for modern TES (16). [This estimate follows from the near-field relation of $E = (Z_0/2) \tan(\theta) d J_z$, where J_z is the current density and Z_0 is the vacuum impedance (14).] In view of the unique potential of this approach for quantitative and phase-resolved information, it is highly desirable to extend this approach to atomic-scale interfaces.

Here, we demonstrate measurement of the ultrafast current that flows less than 0.7 nm across a van der Waals (vdW) interface by recording the emitted transient electromagnetic (EM) radiation. We use prototypical heterostructures of two monolayer transition metal dichalcogenides (TMDCs) (17, 18). Because of the weak vdW interaction between the layers, monolayers of different TMDCs can be isolated and stacked almost arbitrarily to make vertical heterostructures with diverse properties and functionalities (1, 19–21). Of particular interest is the realization of type II band alignment (22), e.g., in heterostructures of monolayer MoS_2 and WS_2: The conduction band minimum of the heterostructure is in the MoS_2 layer, and the valence band maximum is in the WS_2 layer (5, 6, 23, 24). Photogenerated electrons and holes will thus separate into different layers, giving rise to a net current that flows over the subnanometer separation between the MoS_2 and WS_2 monolayers (Fig. 1A) (25). Previous optical pump-probe measurements have suggested that this charge transfer can be as fast as 50 fs (5), making it an ideal candidate for TES.

RESULTS

Experimental

In our investigation, we excited the TMDC heterostructures with femtosecond optical pulses and measured the emitted THz radiation (Fig. 1B) (26). We first examined heterostructures of MoS_2 and WS_2, created from large-area polycrystalline monolayers grown by chemical vapor deposition (CVD). We prepared heterostructures with both stacking orders, namely, MoS_2/WS_2 (MoS_2 transferred onto WS_2)

[1]Department of Applied Physics, Stanford University, Stanford, CA 94305, USA. [2]Stanford Institute for Materials and Energy Sciences, SLAC National Accelerator Laboratory, Menlo Park, CA 94025, USA. [3]Department of Materials Science and Engineering, Stanford University, Stanford, CA 94305, USA. [4]Department of Materials Science and Engineering, North Carolina State University, Raleigh, NC 27695, USA.
*These authors contributed equally to this work.
†Corresponding author. Email: tony.heinz@stanford.edu

and WS$_2$/MoS$_2$ on sapphire substrates. The ultrafast optical pump beam, with a maximum pulse energy of 20 nJ and an angle of incidence of 60°, was lightly focused to an area of ~0.3 mm × 0.6 mm on the sample for studies at low fluence. The 3.1-eV pump photon energy lies well above the optical gaps of both monolayers (23, 25) and is absorbed strongly in both materials. The THz radiation from the interfacial currents, which emerges in the direction of the specular reflection of the pump beam according to the Huygens-Fresnel principle (14), was recorded using free-space electro-optic (EO) sampling (fig. S1) (9, 10). We experimentally determined the properties of the THz emission, from which we extracted quantitative information about the dynamics of interfacial charge transfer and, for excitation at high fluence with a more tightly focused pump beam, its saturation characteristics. We further examined the dependence of charge transfer on the excitation photon energy in MoS$_2$/MoSe$_2$ heterostructures, which allowed us to create initial conditions with hot carriers in both materials (3.1-eV excitation) and resonant band-edge excitons in one monolayer (1.55-eV excitation). All experiments were carried out at room temperature in a nitrogen environment. Further details are presented in Materials and Methods.
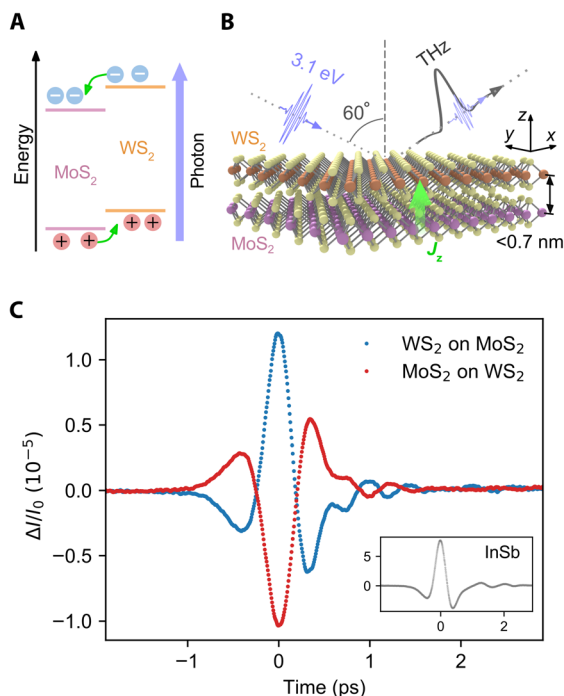
Recording subnanometer interfacial currents by THz emission

Upon photoexcitation by ultrafast optical pulses, we detected bursts of THz radiation from heterostructures of MoS$_2$ and WS$_2$ (Fig. 1C). We did not observe any emission from bare monolayers of either material, nor for excitation of the heterostructure with 1.55-eV sub-gap

photons. These observations show that the THz emission arises from interfacial transfer of photogenerated carriers in the heterostructure, rather than, e.g., from surface adsorbates or optical rectification (27). We calibrated the polarity of the measured THz electric field using emission from a bulk InSb crystal, in which a transient current is known to flow toward the surface through the photo-Dember effect (Fig. 1C, inset) (28).

The THz emission arises from a transient current flowing from the MoS$_2$ to WS$_2$ monolayer in heterostructures of both stacking orders. Exciting WS$_2$/MoS$_2$ heterostructures produces a near–half-cycle pulse with a positive maximum (blue trace in Fig. 1C), indicating a net transient current flowing from MoS$_2$ on the bottom to WS$_2$ on top, as expected (Fig. 1A). The measured THz waveform for the inverted MoS$_2$/WS$_2$ heterostructure has precisely the same shape and amplitude, but the opposite sign, again indicating current from MoS$_2$ to WS$_2$ (red trace in Fig. 1C). These observations are robust and reproduced in heterostructures made with different syntheses and assembly methods (fig. S2). For this dataset, the apparent width of the THz peak (~400 fs) is limited by the duration of the excitation pulse (~200 fs) and the detection bandwidth (~2.5 THz) (29), which also gives rise to the oscillations in the waveform at later times. These limitations are addressed below by high-bandwidth measurements.

The electric field strength of the THz emission was found to scale linearly with excitation fluence for low to moderate fluences (Fig. 2A). This behavior is expected in a regime where the photocarrier density and interfacial current are proportional to the pump fluence. Saturation has not set in for pump fluences up to ~13 μJ cm^{-2} or an induced e-h density of ~5 × 10^{12} cm^{-2}. Deviations from linearity, which arise at higher fluences, are discussed in detail below. On the other hand, for fixed excitation energy, the peak THz field exhibits a sinusoidal modulation as a function of the pump polarization (Fig. 2B). This result

Fig. 1. Recording subnanometer interfacial currents by THz emission. (A) Schematic of the type II band alignment in a WS$_2$/MoS$_2$ heterostructure. Photogenerated electrons and holes separate into different layers, giving rise to a net current that flows from the MoS$_2$ to WS$_2$ monolayer. **(B)** An optically triggered interfacial current J_z from the TMDC heterostructure emits a transient EM pulse at THz frequencies. **(C)** Emitted THz electric field waveforms from WS$_2$/MoS$_2$ and MoS$_2$/WS$_2$ heterostructures upon excitation with 3.1-eV femtosecond pulses as recorded using EO sampling. Inset: Calibration THz waveform from a bulk InSb crystal under identical conditions.
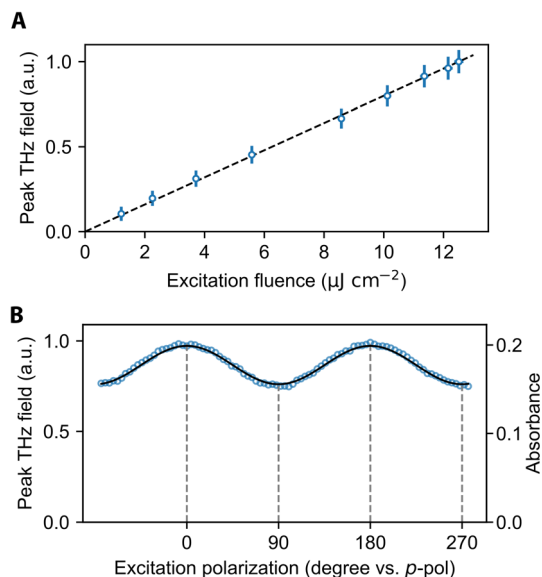

Fig. 2. Scaling of THz emission at low to moderate excitation fluences. (A) Dependence of peak THz field on excitation fluence. The dashed line is a linear fit, which applies for low to moderate fluences. The regime of saturated response is shown in Fig. 4. **(B)** Dependence of peak THz field on excitation polarization. The black curve is the calculated polarization-dependent absorbance of the heterostructure. These results demonstrate that the peak THz field is proportional to the absorbed excitation energy for low to moderate fluences. a.u., arbitrary units.

reflects the polarization dependence of the absorption by the heterostructure, as calculated using known material dielectric functions (black curve in Fig. 2B).

Dynamics and efficiency of interfacial charge transfer

Having established the origin and basic properties of the measured THz emission, we performed high-bandwidth measurements and quantitative simulations to determine the characteristic time scale and efficiency of the charge transfer. At some expense of signal-to-noise ratio, we could shorten the excitation pulse to ~40 fs and increase the EO detection bandwidth to ~7.5 THz. The recorded THz waveform then exhibits bandwidth up to 7 THz (fig. S3). The dominant feature has a width of <200 fs [full width at half maximum (FWHM)] and displays much less deviation from a half cycle (Fig. 3A) than was seen in the lower-bandwidth measurements. Qualitatively, we immediately recognize that charge transfer must occur on a time scale of ~100 fs or less. Below, we analyze the
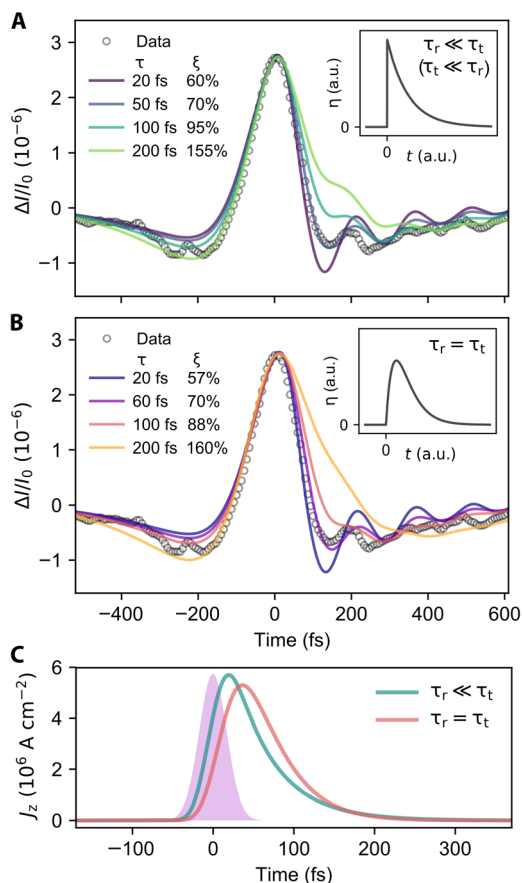
Fig. 3. Determination of the characteristic time scales and efficiency for charge transfer. (**A**) High-bandwidth EO sampling data overlaid with simulations for various combinations of the characteristic material response time $\tau = \tau_r + \tau_t$ and transfer efficiency ξ, as discussed in the text, assuming $\tau_r \ll \tau_t$ (or $\tau_t \ll \tau_r$). Inset: Corresponding impulse response of interfacial current η. (**B**) Same as in (A), but for the case of $\tau_r = \tau_t$. The impulse functions are shown in the inset with the same scales and values for τ and ξ. (**C**) Temporal evolution of the current $J_z(t)$ for the best-fit parameters: $\tau_r \ll \tau_t = 50$ fs and $\tau_r = \tau_t = 30$ fs, both with $\xi = 70\%$. The temporal profile of the excitation pulse used in the experiment is shown in purple in arbitrary units.

experimental electric field waveform more quantitatively based on a model of the charge transfer process and the experimental instrument response.

We first consider the interfacial current density $J_z(t)$ for impulsive optical excitation at $t = 0$. For 3.1-eV above-gap excitation, we expect rapid dynamics involving both intralayer cooling and interlayer transfer of carriers (30, 31), as dictated by the type II band alignment of the heterostructure. The presence of these two processes could lead to a finite rise time of the net interfacial current following excitation. While the full process could be treated using energy- and momentum-dependent scattering rates into all relevant states, this modeling is beyond the scope of this work. Instead, we introduce a simple three-state effective model, which captures the essential physics: Photogenerated electrons (holes) initially relax to an intermediate state at a rate $1/\tau_r$ before subsequently transferring to the other layer at a rate $1/\tau_t$. The net interfacial current is only generated by the second process, which is assumed to be scaled by an overall efficiency factor ξ to account for loss channels, such as radiative recombination. This simple model gives rise to the impulse response for one e-h pair of $\eta(t) = \xi (\tau_t - \tau_r)^{-1} (\exp(-t/\tau_t) - \exp(-t/\tau_r))$. In the limit of resonant pumping of the lowest-energy excitonic transition, as in many previously reported pump-probe experiments, there is no need to consider intralayer relaxation (i.e., $\tau_r \ll \tau_t$) and the impulse response is just exponential decay $\eta(t) \approx \xi \tau_t^{-1} \exp(-t/\tau_t)$ (Fig. 3A, inset). By symmetry, the same form describes the relaxation-limited case ($\tau_t \ll \tau_r$). On the other hand, for $\tau_r \approx \tau_t$, we have $\eta(t) \approx \xi \tau_t^{-1} (t/\tau_t) \exp(-t/\tau_t)$, which represents the strongest deviation from exponential decay (Fig. 3B, inset). We therefore examine the two limiting cases of $\tau_r \ll \tau_t$ and $\tau_r \approx \tau_t$ to infer possible values of τ_r, τ_t, and ξ compatible with our experiment.

To obtain a predicted experimental interfacial current $J_z(t)$, we simply convolute the impulse response $\eta(t)$ and the temporal profile of the excitation pulse. We then use Maxwell's equations to predict the near-surface THz field $E(t)$ and existing models to describe its subsequent propagation and detection (14, 29). We examine simulated waveforms as a function of a characteristic width $\tau = \tau_r + \tau_t$ for the impulse response $\eta(t)$ and of the transfer efficiency ξ.
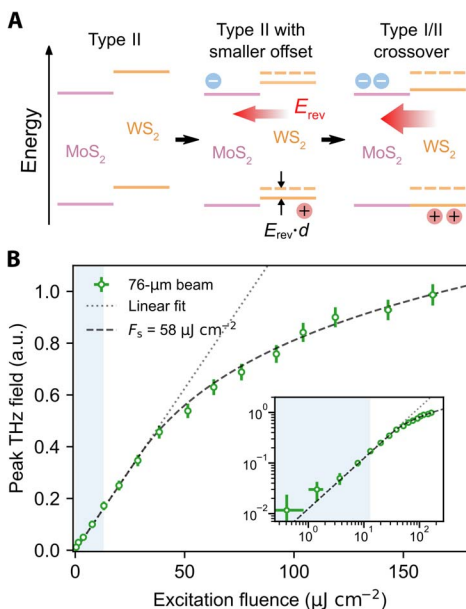
We plot simulations that fit the main peak of the measured waveform for various combinations of τ and ξ for $\tau_r \ll \tau_t$ (Fig. 3A) and $\tau_r = \tau_t$ (Fig. 3B). In both cases, it is apparent that significant deviations from the experimentally measured waveform occur for values of $\tau > 100$ fs, which would also require very large (and even unphysical) values of ξ. The values of $\tau_r \ll \tau_t = 50$ fs (or, by symmetry, $\tau_t \ll \tau_r = 50$ fs) and $\tau_r = \tau_t = 30$ fs ($\tau = 60$ fs) give rise to the best overall fit with $\xi = 70\%$. We note that we are still close to measuring the instrument response and therefore cannot distinguish between the two limiting cases. Nonetheless, we can conclude that both relaxation and net interlayer transfer must occur within a few tens of femtoseconds. Moreover, the charge transfer is not only fast but also highly efficient, with ξ on the order unity. In both limits, the inferred current density $J_z(t)$ for a pump fluence of 11 μJ cm^{-2} reaches a value of 5 MA cm^{-2} (Fig. 3C), corresponding to a peak near-surface THz field of ~6 V cm^{-1}.

Saturation of interfacial charge transfer

Next, we explore the saturation of charge transfer at higher excitation fluences. To access higher fluences, we focused the 0.3-mm-diameter excitation beam down to 76 μm. This small beam size gives rise to stronger diffraction loss for the lower-frequency THz components and is therefore less suitable for quantitative recovery of the current profile. Nonetheless, the peak THz field remains a good measure of the interfacial current amplitude because the normalized electric field waveforms remain unchanged up to the highest fluence (fig. S8).

Saturation in the charge transfer sets in when the applied fluence exceeds ~50 μJ cm^{-2} (Fig. 4). To understand the origin of this effect, we first rule out saturation of the absorption as a major contributor. We directly confirm the lack of saturation in the absorption by the constant reflectance of the sample observed up to the highest fluence (fig. S9). The lack of absorption saturation reflects the rapid carrier relaxation expected for excitation at 3.1 eV. The constancy of the reflectance with fluence also indicates that heating effects do not play a significant role over the relevant range of fluences.

On the other hand, as interfacial charge transfer proceeds, a reverse electric field develops that acts to compensate the type II band offset until a type I (nested) band alignment is approached, at which point further net charge transfer will stop (Fig. 4A). We introduce a simple model to describe this phenomenon. We treat the local charge transfer as linear in excitation fluence up to a saturation value F_s, where it ceases to grow. Taking into account the Gaussian intensity profile of the excitation beam, we then fit the data with two free parameters: the low-fluence proportionality constant (i.e., the slope in linear fit) and the saturation fluence F_s (see Materials and Methods). We find $F_s = 58$ μJ cm^{-2}, which translates to a transferred charge density of $\sigma_t = 1.3 \times 10^{13}$ cm^{-2} (16% absorption for the near s-polarized excitation and a 70% transfer efficiency). Assuming an out-of-plane dielectric screening of $\varepsilon_\perp = 10$ in the TMDC heterostructure, this charge density generates a reverse electric field of $E_{rev} = \sigma_t/\varepsilon_0 \varepsilon_\perp = 0.24$ V nm^{-1} and a reverse electric potential of 0.15 V over $d = 0.62$ nm. This is comparable to the ~0.3- to 0.7-eV band offset typically reported in literature (23, 32), with the main source of uncertainty being the

value for $\varepsilon_\perp$. These unavoidable saturation effects may influence the performance achievable in optoelectronic devices involving interfacial charge separation, such as photodetectors and photovoltaics (1). With further refinements in calibration, this saturation also offers a novel route to determine band offsets in heterostructures.

Dependence of interfacial charge transfer on the excitation photon energy

In the measurements described above, we excited the heterostructure with pump photons at energies well above the optical bandgaps in the two materials. To gain further insight into the nature of charge transfer, we have explored how exciting one of the band-edge excitons influences the measured response. To this end, we have investigated a slightly different type II TMDC heterostructure, namely, MoSe$_2$/MoS$_2$, in which the smaller bandgap of MoSe$_2$ allows excitation with both the 3.1- and 1.55-eV photons available from our pump laser (25). For this case, the 3.1-eV photons create hot carriers in both materials, as for the WS$_2$/MoS$_2$ heterostructure examined above, but the 1.55-eV photons create only tightly bound band-edge excitons in MoSe$_2$ (Fig. 5, inset).

The THz waveforms produced by the MoS$_2$/MoSe$_2$ heterostructure for 3.1- and 1.55-eV excitation, normalized by the number of absorbed pump photons, are shown in Fig. 5. In both cases, the near–half-cycle shape with negative maxima implies a transient current flowing from MoS$_2$ on top to MoSe$_2$ on the bottom, consistent with the expected type II band alignment (33). The striking quantitative agreement in shape and amplitude of the THz emission for the two excitation conditions indicates that the rate and efficiency of interlayer charge transfer do not differ significantly between above-gap and resonant excitation within instrument response (~2.5 THz). This result stands in contrast to the substantial dependence on the excitation photon energy of the photoluminescence quantum efficiency (QE) that has been observed in the relevant isolated monolayers (34), for which the QE is found to drop appreciably for higher photon energy. The fact that the charge transfer process in the heterostructure remains equally efficient for higher energy photons suggests that charge transfer is occurring so fast that it competes with relaxation processes within each layer, as suggested recently by mid-infrared spectroscopy (31) and time-dependent density functional theory (35).
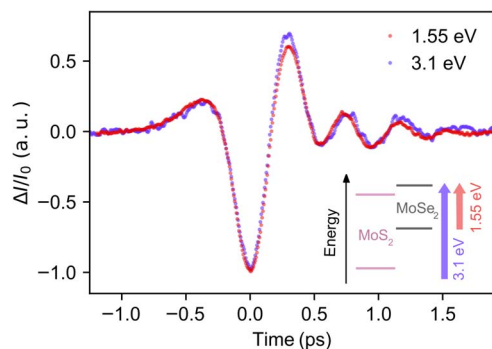

Fig. 4. Saturation of interfacial charge transfer due to buildup of a reverse electric field. (**A**) Schematic of charge transfer saturation due to the buildup of a reverse electric field by the transferred charge that compensates the original band offset. d is the interlayer separation. Net charge transfer ceases to grow when the band alignment crosses over to type I (when the reverse potential completely compensates the smaller of the conduction and valence band offsets). For the purposes of illustration, we fix the MoS$_2$ bands as the reference. (**B**) Dependence of peak THz field on excitation fluence. The blue shaded area is the fluence accessed with the 0.3-mm beam (Fig. 2A). The dotted line is a linear fit using the low-fluence data points, and the dashed line is the saturation fit. The inset shows the same plots presented with logarithmic axes. See the main text and Materials and Methods for details.

Fig. 5. Dependence of the interfacial charge transfer in MoS$_2$/MoSe$_2$ heterostructures on the excitation photon energy. The THz waveforms observed when exciting the heterostructure with 1.55-eV (red) and 3.1-eV (violet) pulses, normalized by the number of absorbed photons, showing no appreciable difference within instrument response. Inset: Schematic of the type II band alignment for a MoS$_2$/MoSe$_2$ heterostructure. 3.1-eV photons excite hot carriers in both materials, while 1.55-eV photons excite only band-edge excitons in MoSe$_2$.

DISCUSSION

In summary, we have demonstrated direct measurement of interfacial currents on the subnanometer length and femtosecond time scale by recording the emitted EM transients. This advance creates unique opportunities not only in the burgeoning field of vdW materials but also for other systems with atomic-scale interfaces (e.g., electrolyte-electrode and adsorbate-solid interfaces). For vdW interfaces, a more detailed study of the photon energy dependence of current flow with high-bandwidth detectors could identify the interplay of intralayer relaxation and interlayer charge transfer, as well as the role of excess energy in loss channels. With appropriate samples, one could, moreover, investigate the dependence of charge transfer dynamics on the relative crystallographic orientation (twist angle) of the two monolayers. This could be carried out not only in heterostructures but also in gated homostructures (36), which would lack distinct spectroscopic features necessary to apply pump-probe techniques. The approach has the potential to be extended with coherent near-field spectroscopy (37) to study charge transfer dynamics with microscopic lateral resolution, as well as the possibility of in situ control of the interlayer contact force and twist angle (38).

MATERIALS AND METHODS

Synthesis and fabrication of TMDC heterostructures

We prepared polycrystalline films of TMDC monolayers with millimeter lateral dimensions on sapphire substrates by CVD. Continuous films of MoS_2 and WS_2 monolayers with small grain size (~100 nm) were synthesized by a self-limiting method (39). Continuous films of MoS_2 monolayer with large grain size (~100 μm) were grown by a different protocol in which molybdenum trioxide (99%, Sigma-Aldrich) and tungsten trioxide (99.99%, Sigma-Aldrich) served as precursors (40). Large isolated triangular domains of $MoSe_2$ (~20 μm, ~40% coverage) were prepared with a similar protocol from molybdenum trioxide (99%, Sigma-Aldrich) and selenium powder (Sigma-Aldrich) precursors.

We used two approaches to make the required vdW heterostructures from the CVD-grown monolayer films. The heterostructures with small-grain MoS_2 and WS_2 were fabricated with standard surface-energy–assisted techniques (41), followed by annealing at 250°C for an hour in 1 atmosphere of Ar. Heterostructures with large-grain MoS_2 were prepared with a modified technique, in which a polydimethylsiloxane (PDMS) stamp (instead of a spin-coated polystyrene film) was used to remove the monolayer from the substrate. The monolayers on the PDMS stamp were subsequently transferred to the target monolayer without the use of solvents. The resulting vdW heterostructures were annealed at 250°C for 2 hours in high vacuum. Heterostructures of $MoS_2/MoSe_2$ were prepared by transferring small-grain MoS_2 onto $MoSe_2$ with the PDMS stamp method, followed by annealing at 270°C for 2 hours in high vacuum. The reflectance contrast and Raman spectra of the heterostructures closely resembled the sum of the spectra of the two separate monolayers, with the expected slight shifts and broadening of the features (fig. S4) (42, 43).

We observed a clear dependence on the stacking order of the layers, as discussed in the main text. Other than the waveform polarity, the THz waveforms were very similar for different samples, irrespective of synthesis or fabrication methods (fig. S2). We note that the excitation beam always illuminated a very large number of grains in both materials with random relative crystallographic orientation.

Experimental apparatus, phase calibration, and bandwidth control

A schematic of the experimental apparatus is presented in fig. S1. Laser excitation away from normal incidence was needed to allow a finite projection of the out-of-plane current in the direction perpendicular to the propagation of the THz wave (Fig. 1B) (14). The 3.1-eV ultrafast laser excitation was produced by second-harmonic generation of a mode-locked Ti:sapphire laser with pulses of 40-fs (FWHM) duration and 5.12-MHz repetition rate in a β-barium borate crystal (1 mm or 200 μm thick for data in Figs. 1 and 2 and Figs. 3 to 5, respectively). The refocused THz radiation from the heterostructure was detected using the EO effect in a noncentrosymmetric crystal (1-mm-thick ZnTe or 258-μm-thick GaP for data in Figs. 1, 2, 4, and 5 and Fig. 3, respectively). The induced birefringence in the EO crystal was recorded at different delay times by a laser probe pulse passing through a polarizing beam-splitter (Wollaston prism) and impinging on a balanced photodetector. The power imbalance (ΔI), which is proportional to the THz electric field, was fed into a lock-in amplifier synchronized with modulation of the excitation beam at 320 kHz by an acousto-optic modulator. By scanning the time delay between the excitation and probe pulses, the temporal profile of the transient THz electric field could be mapped with a time resolution down to ~40 fs.

To determine the direction of the underlying current in the heterostructure, we calibrated the polarity of the measured EO signal using the photo-Dember effect in a bulk (InSb) semiconductor crystal: The photogenerated electrons diffused into the bulk faster than the holes due to their higher mobility, generating a net transient current flowing toward the surface (+z in Fig. 1B) (28). We tuned the phase of the lock-in amplifier so that this +z current corresponded to a near–half-cycle profile with a positive maximum (Fig. 1C, inset).

Optical properties of the heterostructures

To model the optical absorption of MoS_2/WS_2 heterostructures, we treated the MoS_2 and WS_2 layers as independent, with in-plane dielectric functions of 2.5 + 30i and 9 + 23.5i (25) and an out-of-plane dielectric function of 10 at 3.1 eV. The results were not sensitive to the choice of the out-of-plane dielectric function (fig. S5). We used nominal thicknesses of 0.615 and 0.618 nm for MoS_2 and WS_2 monolayers, respectively, and values of 3.19 and 3.16 for the in- and out-of-plane dielectric function of the c-cut sapphire substrate (44). We obtained the absorption of the heterostructure for light incident at 60° and varying polarization. This analysis replicated the measured dependence of the THz radiation on the polarization of the excitation beam, as shown in Fig. 2B. The same calculation also provided the reflectance of the heterostructure: 37.5% for s-polarization and 1.5% for p-polarization. The reflectance for p-polarization was much smaller because the incident angle is close to the Brewster's angle. We expected a reflectance of 36.4% for the near s-polarized excitation (10° toward p-polarization) in the high fluence measurements (Fig. 4), in reasonable agreement with the experimental value of 32% (fig. S9).

We applied the same method to calculate the absorption of $MoS_2/MoSe_2$ heterostructures using dielectric functions of 2.5 + 30i and 5.0 + 15.8i for 3.1 eV, and 21 + 0i and 20.6 + 12.3i for 1.55 eV (25). We used a nominal thickness of 0.646 nm for the $MoSe_2$ monolayer and values of 3.10 and 3.06 for the in- and out-of-plane dielectric function of the sapphire substrate for 1.55 eV. For the measurements in Fig. 5, both the 1.55- and 3.1-eV excitation beams were p-polarized. The calculated p-polarization absorbance for 3.1 eV (17.8%) was about six

times that for 1.55 eV (3.0%) and was taken into account when normalizing the THz waveforms.

Analysis of dynamics and efficiency of interfacial charge transfer

The out-of-plane current density J_z is the convolution (denoted by *) of the excitation pulse and the impulse current response as described in the main text: $J_z(t) = \alpha e\Phi(t) * \eta(t)$, where α is the absorption coefficient of the heterostructure, e is electron charge, and $\Phi(t)$ is the photon flux of the excitation pulse on the sample. The charge transfer efficiency ξ, which is included in the impulse response, is defined as the net electron charge transferred across the vdW interface per absorbed photon. Note that the value of ξ is independent on the respective absorption of the individual layers for a given total absorption, because the interfacial current from a photogenerated electron in WS_2 moving into MoS_2 is equivalent to the effect of a photogenerated hole in MoS_2 moving into WS_2.

The transient electric field immediately above the sample surface was given by the relation $E(t) = \varsigma Z_0 d J_z(t)$ *(14)*, where $\varsigma = 0.108$ is an out-coupling efficiency that depends on the angle of incidence (60°) and the THz dielectric function of the sample ($\varepsilon_{\text{sapphire\_THz}} \sim 10$; for simplicity, we take $\varepsilon_{\text{TMDC}\perp\text{\_THz}} \sim 10$), $Z_0 = 376.73$ ohms is the impedance of free space, and $d = 0.62$ nm is the average distance the current flows. In our measurement, the THz field propagated away from the surface, passed through collection optics of finite size and a high-resistivity Si wafer that blocks the reflected excitation beam, and was refocused at the front surface of the EO crystal. These propagation effects were treated as a high-pass filter that only depends on the geometry of the apparatus and were calibrated experimentally.

Last, we modeled the process of EO sampling by applying the transfer function $G_{\text{EO}}(f) = A_{\text{tr}}(f) d_{\text{EO}}(f) r_{41}(f)$ in frequency domain, where $A_{\text{tr}}(f)$ is the amplitude transmission coefficient of the interface between air and the EO crystal, $d_{\text{EO}}(f)$ is the effective thickness of the EO crystal, taking into account the phase mismatch between the THz pulse and the optical probe pulse, and $r_{41}(f)$ is the frequency-dependent EO coefficient of the material. We followed the procedure in *(29)* with the experimentally determined optical group index ($n_g = 3.57$) and THz refractive index for GaP (fig. S6). The result was then convolved with a normalized probe intensity profile to obtain the final simulation of the measured THz waveform. The total transfer function connecting J_z and $\Delta I/I_0$ for our high-bandwidth apparatus is shown in fig. S7.

Analysis of saturation of interfacial charge transfer

The model used to fit the saturation in charge transfer with increasing laser fluence (Fig. 4) was based on two assumptions: (i) The local peak THz field immediately above the sample surface $E_{\text{pk\_sample}}(r)$ (r is the radial distance from the center of the beam) scales linearly with local excitation fluence $F(r)$ up to F_s, i.e., $E_{\text{pk\_sample}}(r) = \{AF(r), F(r) < F_s; AF_s, F(r) \geq F_s\}$, in which A is the low-fluence proportionality constant and F_s corresponds to the fluence that drives the type II to type I crossover. (ii) The peak field measured by EO sampling $E_{\text{pk\_EO}}$ can be approximated by averaging $E_{\text{pk\_sample}}(r)$ over the illuminated region on the sample. In addition, our excitation beam has a Gaussian intensity profile, and the fluence F_0 we report is the total pulse energy divided by the area within the Gaussian beam diameter ($1/e^2$) projected onto the sample. The peak local fluence at the center of the beam is therefore $2F_0$.

It is then straightforward to show that $E_{\text{pk\_EO}}$ has the following dependence on F_0: $E_{\text{pk\_EO}}(F_0) = \{A'F_0, F_0 < F_s/2; A'F_s[\ln(2F_0/F_s) + 1]/2, F_0 \geq F_s/2\}$, in which A' is the overall low-fluence proportionality

constant. We note that this model is valid if (i) the charge transfer rate and efficiency only weakly depend on the band offset energies as long as the alignment remains type II, (ii) the illuminated area is considerably smaller than the diffraction-limited spot after refocusing, and (iii) F_0 is within few times of F_s. Condition (i) is a simplification motivated by the robustness of ultrafast charge transfer in different types of samples. Conditions (ii) and (iii) depend on experimental setup and are reasonably well satisfied for the measurement conditions relevant for Fig. 4.

SUPPLEMENTARY MATERIALS

Fig. S1. Schematic of the time-domain TES setup.
Fig. S2. Reproducibility of the measurements.
Fig. S3. Comparison between the low- and high-bandwidth data.
Fig. S4. Typical reflectance contrast and Raman spectra of the heterostructures.
Fig. S5. Analysis of the optical properties calculation.
Fig. S6. Determination of THz refractive index of GaP.
Fig. S7. Total transfer function of the setup.
Fig. S8. Normalized THz waveforms for representative excitation fluences.
Fig. S9. Reflected excitation power as a function of excitation fluence.

REFERENCES AND NOTES

1. Q. H. Wang, K. Kalantar-Zadeh, A. Kis, J. N. Coleman, M. S. Strano, Electronics and optoelectronics of two-dimensional transition metal dichalcogenides. *Nat. Nanotechnol.* **7**, 699–712 (2012).
2. F. H. L. Koppens, P. Avouris, A. C. Ferrari, M. S. Vitiello, M. Polini, Photodetectors based on graphene, other two-dimensional materials and hybrid systems. *Nat. Nanotechnol.* **9**, 780–793 (2014).
3. M. Graetzel, R. A. J. Janssen, D. B. Mitzi, E. H. Sargent, Materials interface engineering for solution-processed photovoltaics. *Nature* **488**, 304–312 (2012).
4. C. Zhu, R. E. Usiskin, Y. Yu, J. Maier, The nanoscale circuitry of battery electrodes. *Science* **358**, eaao2808 (2017).
5. X. Hong, J. Kim, S.-F. Shi, Y. Zhang, C. Jin, Y. Sun, S. Tongay, J. Wu, Y. Zhang, F. Wang, Ultrafast charge transfer in atomically thin MoS$_2$/WS$_2$ heterostructures. *Nat. Nanotechnol.* **9**, 682–686 (2014).
6. Z. Ji, H. Hong, J. Zhang, Q. Zhang, W. Huang, T. Cao, R. Qiao, C. Liu, J. Liang, C. Jin, L. Jiao, K. Shi, S. Meng, K. Liu, Robust stacking-independent ultrafast charge transfer in MoS$_2$/WS$_2$ bilayers. *ACS Nano* **11**, 12020–12026 (2017).
7. D. Kozawa, A. Carvalho, I. Verzhbitskiy, F. Giustiniano, Y. Miyauchi, S. Mouri, A. H. Castro Neto, K. Matsuda, K. Eda, Evidence for fast interlayer energy transfer in MoSe$_2$/WS$_2$ heterostructures. *Nano Lett.* **16**, 4087–4093 (2016).
8. J. D. Jackson, R. F. Fox, *Classical Electrodynamics* (Wiley, ed. 3, 1999).
9. A. Nahata, A. S. Weling, T. F. Heinz, A wideband coherent terahertz spectroscopy system using optical rectification and electro-optic sampling. *Appl. Phys. Lett.* **69**, 2321–2323 (1996).
10. Q. Wu, M. Litz, X.-C. Zhang, Broadband detection capability of ZnTe electro-optic field detectors. *Appl. Phys. Lett.* **68**, 2924–2926 (1996).
11. H. Zhong, N. Karpowicz, X.-C. Zhang, Terahertz emission profile from laser-induced air plasma. *Appl. Phys. Lett.* **88**, 261103 (2006).
12. M. C. Beard, G. M. Turner, C. A. Schmuttenmaer, Measuring intramolecular charge transfer via coherent generation of THz radiation. *J. Phys. Chem. A* **106**, 878–883 (2002).
13. X.-C. Zhang, B. B. Hu, J. T. Darrow, D. H. Auston, Generation of femtosecond electromagnetic pulses from semiconductor surfaces. *Appl. Phys. Lett.* **56**, 1011–1013 (1990).
14. J. Shan, T. F. Heinz, in *Ultrafast Dynamical Processes in Semiconductors*, K.-T. Tsen, Ed. (Springer-Verlag, 2004), pp. 1–56.
15. L. Zhang, Y. Huang, Q. Zhao, L. Zhu, Z. Yao, Y. Zhou, W. Du, X. Xu, Terahertz surface emission of d-band electrons from a layered tungsten disulfide crystal by the surface field. *Phys. Rev. B* **96**, 155202 (2017).
16. C. Riek, D. V. Seletskiy, A. S. Moskalenko, J. F. Schmidt, P. Krauspe, S. Eckart, S. Eggert, G. Burkard, A. Leitenstorfer, Direct sampling of electric-field vacuum fluctuations. *Science* **350**, 420–423 (2015).
17. K. F. Mak, C. Lee, J. Hone, J. Shan, T. F. Heinz, Atomically thin MoS$_2$: A new direct-gap semiconductor. *Phys. Rev. Lett.* **105**, 136805 (2010).

18. A. Splendiani, L. Sun, Y. Zhang, T. Li, J. Kim, C. Y. Chim, G. Galli, F. Wang, Emerging photoluminescence in monolayer MoS_2. *Nano Lett.* **10**, 1271–1275 (2010).

19. K. S. Novoselov, A. Mishchenko, A. Carvalho, A. H. Castro Neto, 2D materials and van der Waals heterostructures. *Science* **353**, aac9439 (2016).

20. G. Iannaccone, F. Bonaccorso, L. Colombo, G. Fiori, Quantum engineering of transistors based on 2D materials heterostructures. *Nat. Nanotechnol.* **13**, 183–191 (2018).

21. D. Deng, K. S. Novoselov, Q. Fu, N. Zheng, Z. Tian, X. Bao, Catalysis with two-dimensional materials and their heterostructures. *Nat. Nanotechnol.* **11**, 218–230 (2016).

22. C.-H. Lee, G.-H. Lee, A. M. van der Zande, W. Chen, Y. Li, M. Han, X. Cui, G. Arefe, C. Nuckolls, T. F. Heinz, J. Guo, J. Hone, P. Kim, Atomically thin p–n junctions with van der Waals heterointerfaces. *Nat. Nanotechnol.* **9**, 676–681 (2014).

23. H. M. Hill, A. F. Rigosi, K. T. Rim, G. W. Flynn, T. F. Heinz, Band alignment in MoS_2/WS_2 transition metal dichalcogenide heterostructures probed by scanning tunneling microscopy and spectroscopy. *Nano Lett.* **16**, 4831–4837 (2016).

24. K. Kośmider, J. Fernández-Rossier, Electronic properties of the MoS_2-WS_2 heterojunction. *Phys. Rev. B* **87**, 075451 (2013).

25. Y. Li, A. Chernikov, X. Zhang, A. Rigosi, H. M. Hill, A. M. van der Zande, D. A. Chenet, E.-M. Shih, J. Hone, T. F. Heinz, Measurement of the optical dielectric function of monolayer transition-metal dichalcogenides: MoS_2, $MoSe_2$, WS_2, and WSe_2. *Phys. Rev. B* **90**, 205422 (2014).

26. B. Guzelturk, R. A. Belisle, M. D. Smith, K. Bruening, R. Prasanna, Y. Yuan, V. Gopalan, C. J. Tassone, H. I. Karunadasa, M. D. McGehee, A. M. Lindenberg, Terahertz emission from hybrid perovskites driven by ultrafast charge separation and strong electron–phonon coupling. *Adv. Mater.* **30**, 1704737 (2018).

27. Y. Huang, L. Zhu, Q. Zhao, Y. Guo, Z. Ren, J. Bai, X. Xu, Surface optical rectification from layered MoS_2 crystal by THz time-domain surface emission spectroscopy. *ACS Appl. Mater. Interfaces* **9**, 4956–4965 (2017).

28. P. Gu, M. Tani, S. Kono, K. Sakai, X.-C. Zhang, Study of terahertz radiation from InAs and InSb. *J. Appl. Phys.* **91**, 5533–5537 (2002).

29. S. Casalbuoni, H. Schlarb, B. Schmidt, P. Schmüser, B. Steffen, A. Winter, Numerical studies on the electro-optic detection of femtosecond electron bunches. *Phys. Rev. ST Accel. Beams* **11**, 072802 (2008).

30. A. Grubišić Čabo, J. A. Miwa, S. S. Grønborg, J. M. Riley, J. C. Johannsen, C. Cacho, O. Alexander, R. T. Chapman, E. Springate, M. Grioni, J. V. Lauritsen, P. D. C. King, P. Hofmann, S. Ulstrup, Observation of ultrafast free carrier dynamics in single layer MoS_2. *Nano Lett.* **15**, 5883–5887 (2015).

31. H. Chen, X. Wen, J. Zhang, T. Wu, Y. Gong, X. Zhang, J. Yuan, C. Yi, J. Lou, P. M. Ajayan, W. Zhuang, G. Zhang, J. Zheng, Ultrafast formation of interlayer hot excitons in atomically thin MoS_2/WS_2 heterostructures. *Nat. Commun.* **7**, 12512 (2016).

32. C. Zhang, C. Gong, Y. Nie, K.-A. Min, C. Liang, Y. Jun Oh, H. Zhang, W. Wang, S. Hong, L. Colombo, R. M. Wallace, K. Cho, Systematic study of electronic structure and band alignment of monolayer transition metal dichalcogenides in Van der Waals heterostructures. *2D Mater.* **4**, 015026 (2017).

33. F. Ceballos, M. Z. Bellus, H.-Y. Chiu, H. Zhao, Ultrafast charge separation and indirect exciton formation in a MoS_2–$MoSe_2$ van der Waals heterostructure. *ACS Nano* **8**, 12717–12724 (2014).

34. D. Kozawa, R. Kumar, A. Carvalho, K. Kumar Amara, W. Zhao, S. Wang, M. Toh, R. M. Ribeiro, A. H. Castro Neto, K. Matsuda, G. Eda, Photocarrier relaxation pathway in two-dimensional semiconducting transition metal dichalcogenides. *Nat. Commun.* **5**, 4543 (2014).

35. J. Zhang, H. Hong, J. Zhang, H. Fu, P. You, J. Lischner, K. Liu, E. Kaxiras, S. Meng, New pathway for hot electron relaxation in two-dimensional heterostructures. *Nano Lett.* **18**, 6057–6063 (2018).

36. Y. Cao, V. Fatemi, S. Fang, K. Watanabe, T. Taniguchi, E. Kaxiras, P. Jarillo-Herrero, Unconventional superconductivity in magic-angle graphene superlattices. *Nature* **556**, 43–50 (2018).

37. V. Kravtsov, R. Ulbricht, J. M. Atkin, M. B. Raschke, Plasmonic nanofocused four-wave mixing for femtosecond near-field imaging. *Nat. Nanotechnol.* **11**, 459–464 (2016).

38. R. Ribeiro-Palau, C. Zhang, K. Watanabe, T. Taniguchi, J. Hone, C. R. Dean, Twistable electronics with dynamically rotatable heterostructures. *Science* **361**, 690–693 (2018).

39. Y. Yu, C. Li, Y. Liu, L. Su, Y. Zhang, L. Cao, Controlled scalable synthesis of uniform, high-quality monolayer and few-layer MoS_2 films. *Sci. Rep.* **3**, 1866 (2013).

40. Y. Yu, S. Hu, L. Su, L. Huang, Y. Liu, Z. Jin, A. A. Purezky, D. B. Geohegan, K. Wook Kim, Y. Zhang, L. Cao, Equally efficient interlayer exciton relaxation and improved absorption in epitaxial and nonepitaxial MoS_2/WS_2 heterostructures. *Nano Lett.* **15**, 486–491 (2015).

41. A. Gurarslan, Y. Yu, L. Su, Y. Yu, F. Suarez, S. Yao, Y. Zhu, M. Ozturk, Y. Zhang, L. Cao, Surface-energy-assisted perfect transfer of centimeter-scale monolayer and few-layer MoS_2 films onto arbitrary substrates. *ACS Nano* **8**, 11522–11528 (2014).

42. A. F. Rigosi, H. M. Hill, Y. Li, A. Chernikov, T. F. Heinz, Probing interlayer interactions in transition metal dichalcogenide heterostructures by optical spectroscopy: MoS_2/WS_2 and $MoSe_2/WSe_2$. *Nano Lett.* **15**, 5033–5038 (2015).

43. X. He, H. Li, Z. Zhu, Z. Dai, Y. Yang, P. Yang, Q. Zhang, P. Li, U. Schwingenschlogl, X. Zhang, Strain engineering in monolayer WS_2, MoS_2, and the WS_2/MoS_2 heterostructure. *Appl. Phys. Lett.* **109**, 173105 (2016).

44. I. H. Malitson, Refraction and dispersion of synthetic sapphire. *J. Opt. Soc. Am.* **52**, 1377 (1962).